Geophysical Research Letters

RESEARCH LETTER
10.1029/2023GL103836

Satellite Evidence of $HONO/NO_2$ Increase With Fire Radiative Power

C. D. Fredrickson[1], N. Theys[2], and J. A. Thornton[1]

[1]Department of Atmospheric Sciences, University of Washington, Seattle, WA, USA, [2]Royal Belgian Institute for Space Aeronomy (BIRA-IASB), Brussels, Belgium

Key Points:

- We report TROPOspheric Monitoring Instrument nitrous acid, nitrogen dioxide, and the ratio of nitrous acid to nitrogen dioxide during the Australian Black Summer
- Mean nitrous-acid-to-nitrogen-dioxide ratio shows an increasing relationship with mean fire radiative power both in Australia and globally
- The relationship between nitrous-acid-to-nitrogen-dioxide ratio and fire radiative power is affected by vegetation type

Supporting Information:

Supporting Information may be found in the online version of this article.

Correspondence to:

J. A. Thornton,
joelt@uw.edu

Citation:

Fredrickson, C. D., Theys, N., & Thornton, J. A. (2023). Satellite evidence of $HONO/NO_2$ increase with fire radiative power. *Geophysical Research Letters*, *50*, e2023GL103836. https://doi.org/10.1029/2023GL103836

Received 31 MAR 2023
Accepted 8 JUN 2023

Author Contributions:

Conceptualization: C. D. Fredrickson, J. A. Thornton
Data curation: N. Theys
Formal analysis: C. D. Fredrickson
Funding acquisition: C. D. Fredrickson
Investigation: C. D. Fredrickson, N. Theys
Methodology: C. D. Fredrickson, N. Theys, J. A. Thornton
Resources: N. Theys
Software: C. D. Fredrickson
Supervision: J. A. Thornton

Abstract Wildfires are important sources of atmospheric reactive nitrogen. The reactive nitrogen species partitioning generally depends on fire characteristics. One reactive nitrogen compound, nitrous acid (HONO), is a source of hydroxyl radicals and nitric oxide, which can impact the oxidizing capacity of the atmosphere and fire plume chemistry and composition. We study the Australian wildfire season of 2019–2020, known as Black Summer, where numerous large and intense wildfires burned throughout the continent. We use HONO and nitrogen dioxide (NO_2) from the TROPOspheric Monitoring Instrument (TROPOMI) and fire radiative power (FRP) from the Visible Infrared Imaging Radiometer Suite to investigate HONO and NO_2 relationships with fire characteristics. The ratio of HONO to NO_2 increases linearly with FRP both in Australia and globally. Both Australian and global fire relationships depend strongly on land cover type. These relationships can be applied to emission inventories to improve wildfire emission representation in models.

Plain Language Summary During the southern hemisphere summer from 2019 to 2020, colloquially known as the Black Summer, multiple wildfires burned throughout Australia that caused widespread environmental, ecological, and property damage. The smoke and gases from the wildfires contributed to poor air quality and impacted stratospheric ozone chemistry. One gas that wildfires emit is nitrous acid, a nitrogen-containing molecule that breaks down under sunlight to create reactive species. These reactive species undergo rapid chemical transformations that ultimately lead to the creation of pollutants, such as ozone and particulate matter. Nitrous acid is emitted alongside nitrogen dioxide from wildfire smoke, but the amounts emitted depend on fire characteristics. Multiple satellites were able to measure nitrous acid, nitrogen dioxide, and fire power during the Black Summer. By counting each smoke pixel and computing summary statistics, we found an increasing, linear relationship between the ratio of nitrous acid to nitrogen dioxide and fire power. Satellites can also characterize the type of ecosystem that is burning. With this information, we derived relationships over three ecosystem types, which can be extended globally. This relationship can be included in computer models that simulate the chemistry of the atmosphere and the impacts of wildfire emissions.

1. Introduction

Atmospheric nitrous acid (HONO) is an important source of the hydroxyl radical (OH) through rapid photolysis, where HONO lifetime can be as short as 10–20 min at noon under clear-sky conditions (Barney et al., 2000; W. R. Stockwell & Calvert, 1978). OH is the main initiator of oxidative degradation in the atmosphere, for example, of reduced non-radical compounds such as methane and carbon monoxide. By altering the atmosphere's oxidative capacity, HONO impacts secondary chemical pathways leading to ozone, peroxyacetyl nitrate, and secondary particulate matter (Gil et al., 2021; J. Zhang et al., 2020; S. Zhang et al., 2021).

HONO is directly emitted from combustion sources. Recently, scientists have been interested in HONO emitted from fires (Bourgeois et al., 2022; Lindaas et al., 2021; Peng et al., 2020). In the United States, both the number of large wildfires and the total burned area per year have been increasing and continued global warming is predicted to increase the very large fire potential by midcentury (Barbero et al., 2015; Dennison et al., 2014). Thus, fires are expected to become increasingly important sources of HONO. In addition to HONO, fires emit nitrogen oxide radicals such as nitric oxide (NO) and nitrogen dioxide (NO_2). The partitioning of reactive nitrogen emissions from wildfires between HONO and NO_x ($NO + NO_2$) is of interest because HONO's production of OH can change the near-field chemistry and thus the fate of short-lived gases within wildfire plumes. However, there is a limited understanding of what determines this partitioning. A few studies have investigated the role of fuel characteristics

Visualization: C. D. Fredrickson
Writing – original draft: C. D. Fredrickson
Writing – review & editing: N. Theys, J. A. Thornton

and combustion conditions on partitioning of reactive nitrogen emissions (Burling et al., 2010; Chai et al., 2019; Chen et al., 2010; Coggon et al., 2016; Roberts et al., 2020; C. E. Stockwell et al., 2014). However, most of these studies rely on laboratory burns, which are not representative of the real atmosphere, and some studies do not isolate HONO. No previous study has investigated the relationship between fire activity and reactive nitrogen partitioning. After emission, the partitioning of HONO and NO_x depends upon available sunlight, dilution rates, and secondary chemistry (Juncosa Calahorrano et al., 2021; Peng et al., 2020, 2022; Wang et al., 2021).

HONO from fires in the field has primarily been measured in situ (Müller et al., 2016; Neuman et al., 2016; Peng et al., 2020; Rondon & Sanhueza, 1989; Yokelson et al., 2007, 2009), but these measurements have limited spatial coverage and are not sampled regularly enough to build informative statistics. Alternatively, HONO can be measured remotely using its spectroscopic properties. Recent advances in satellite retrievals have allowed HONO to be detected with TROPOspheric Monitoring Instrument (TROPOMI) (Theys et al., 2020). Satellite remote sensing has the benefit of having access to freshly emitted plumes directly over the fires, providing long-term observations with increased spatial and temporal sampling relative to in situ observations. However, satellite sounding through optically thick fire plumes makes quantitative interpretations of remotely sensed ultraviolet (UV) and visible spectra challenging (Bousserez, 2014; Lin et al., 2015; Rowe et al., 2022).

The 2019–2020 Australian bushfire season, known as the Black Summer, was an unprecedented occurrence of numerous, intense wildfires nationwide that greatly impacted tropospheric and stratospheric chemistry (Bernath et al., 2022; Mouat et al., 2022; Peterson et al., 2021; Simmons et al., 2022; Solomon et al., 2022, 2023). TROPOMI was operational during Black Summer and provided a rich chemical data set of these fires. Using TROPOMI and Visible Infrared Imaging Radiometer Suite (VIIRS) observations over Australia during the 2019–2020 Black Summer, we examine the relationships between the ratio of HONO to NO_2 (HONO/NO_2), fire radiative power (FRP), absorbing aerosol, and land (fuel) type. We show that our findings over Australia are similar to global fires, and suggest these relationships need to consider land type to improve biomass burning emission inventories of HONO for use in global chemical transport models, where currently, no FRP-based emission inventory quantifies HONO, only NO_x, through a constant land cover type emission factor.

2. Data and Methods

2.1. TROPOMI

TROPOMI is a hyperspectral imaging spectrometer providing measurements of atmospheric composition. It was launched into space on 13 October 2017, on the Sentinel-5 Precursor (S-5P) satellite. The spatial resolution of TROPOMI at nadir is $3.5 \times 5.5\ km^2$ which became standard on 6 August 2019. S-5P crosses the equator in its ascending mode at 1:30 p.m. Mean Local Solar Time. Measurements of HONO and NO_2 from TROPOMI used in this analysis are obtained by applying the Differential Optical Absorption Spectroscopy (DOAS) method (Platt & Stutz, 2008). The results of DOAS are slant column densities (SCDs) (i.e., the integrated concentration along the mean light path) of several trace gases, and other fitted parameters. Here, both HONO SCDs and NO_2 SCDs are derived from the UV spectral range from 337 to 375 nm, as described by Theys et al. (2020). Additionally, the NO_2 SCDs are corrected to remove the background (mostly stratospheric) component via a latitudinal parameterization in a clean sector over the Pacific Ocean. Presently, the vertical column densities (VCDs) of HONO and of NO_2 are not computed, as the scaling factors (so-called air mass factors) necessary to convert SCDs into VCDs are rather uncertain under large aerosol loadings. Instead, we use the ratio of HONO SCD to NO_2 SCD to cancel out air mass factors. Doing so, we assume that HONO and NO_2 have nearly identical air mass factors due to their retrieval in the same wavelength window and have similar interactions with aerosols (Theys et al., 2020). As such, our analysis and conclusions focus on the ratio of temporally- and spatially-collocated HONO SCDs and NO_2 SCDs (HONO/NO_2) than on the SCDs alone. Historically, HONO/NO_x is an established indicator of photochemical HONO production, but has also assessed fuel nitrogen content and burn conditions of wildfires (Burling et al., 2010; Elshorbany et al., 2012; Kleffmann, 2007; Peng et al., 2020).

In a first step, we analyzed TROPOMI data during austral summer from 1 September 2019 to 31 January 2020 and selected for a region containing Australia, ranging latitudinally from 50°S to 10.58°S and longitudinally from 100°E to 180°E. To extend our analysis to the entire globe, we have then analyzed the TROPOMI data set provided as Supporting Information in Theys et al. (2020) which covers fires detected between 1 May 2018 and 30 April 2019.

We also used TROPOMI's standard Ultraviolet Aerosol Index (UVAI) product (Stein Zweers, 2022), which exploits the spectral contrast with respect to a pure Rayleigh atmosphere to detect aerosols. Positive values of this index indicate absorbing particles and is referred to as the Absorbing Aerosol Index. This index can capture both dust and biomass burning particles. When the UVAI product is negative, it is indicative of predominantly scattering particles (Penning de Vries et al., 2009).

2.2. Data on Fire Activity and Land Type

To locate fires across Australia, we accessed the Suomi National Polar-orbiting Partnership (Suomi NPP) VIIRS 375 m active fire detection standard product provided by the National Aeronautics and Space Administration's (NASA) Fire Information for Resource Management System (FIRMS) (Schroeder, 2020; Schroeder et al., 2014). This product reports geolocated FRP along with data quality and other data characteristics. Uncertainties in FRP can result from partly-filled satellite pixels, smoke opacity above the fire, and non-unit fire emissivity (Schroeder et al., 2010; Souri et al., 2017). We assume that partly-filled VIIRS pixels will occur over the entire FRP range and its effect will be systematic when binning the data (i.e., a translation along the FRP axis), but should not change the conclusion that $HONO/NO_2$ increases with FRP. Suomi NPP provides local measurements twice a day where the daytime equatorial crossing time is 1:30 p.m. Mean Local Solar Time. The Suomi NPP leads the S-5P by 3.5 min making comparisons between the two data sets nearly seamless in time. We analyzed VIIRS data during the same period and geographical boundaries as for TROPOMI described above.

To evaluate the role of different land cover types on the $HONO/NO_2$ relationships, we used the Terra and Aqua combined Moderate Resolution Imaging Spectroradiometer (MODIS) Land Cover Type (MCD12Q1) Version 6 yearly data product (Friedl & Sulla-Menashe, 2019) for the year 2019. This is a level 3 global data product with a spatial resolution of 500 m on the sinusoidal grid. We use the Annual International Geosphere-Biosphere Programme (IGBP) land cover type encoding. The land cover type encoding was sampled at TROPOMI pixel centers. There are 17 land cover type categories. For our analysis, the grouped categories are: (a) grassland and savanna, (b) open and closed shrubland, and (c) needleleaf and broadleaf evergreen.

2.3. TROPOMI Data Filtering and Analysis Method

Not all data collected from TROPOMI and VIIRS was included in this analysis. For TROPOMI pixels in our study area and period, we selected those that had both positive UVAI to capture smoke-impacted areas and contained at least one VIIRS fire detection. The fire detection pixels were a subset of the complete VIIRS data set and fulfilled five criteria: (a) labeled as vegetation fires, (b) FRPs greater than 50 MW, (c) detection with nominal or high confidence, (d) detection during daytime, and (e) detection within 25 min of the TROPOMI pixels. Condition (b) was determined due to TROPOMI's detection limits (see Figures 2b and 2c) (Theys et al., 2020). Condition (e) was selected to be between the satellites' train time lag (3.5 min) and their orbit times (101 min).

For every TROPOMI pixel that passed the pixel filtering, we calculated multiple descriptive statistics of surrounding VIIRS FRP pixels and surrounding UVAI >0 TROPOMI pixels. More specifically, we performed statistics on TROPOMI 3×3 neighboring pixels and on VIIRS fire pixels within the same region. We use the 3×3 neighboring pixels to capture nearby smoke that was transported by the wind and to reduce high variability in $HONO/NO_2$ in individual pixels. Figure S1 in Supporting Information S1 demonstrates our pixel analysis method for the Kangaroo Fire on 3 January 2020. We report on the weighted-mean $HONO/NO_2$, weighted-mean HONO SCD, weighted-mean NO_2 SCD, and unweighted-mean FRP, all hereafter referred to as mean $HONO/NO_2$, mean HONO SCD, etc. Weighted-mean $HONO/NO_2$ is computed as the average of ratios. The weighting methodology is found in Text S1 in Supporting Information S1. The results from this TROPOMI-pixel-focused analysis method remain the same if we perform an analogous VIIRS-pixel-focused analysis method.

For the global analysis of the supplementary TROPOMI data set, we slightly adapted the approach. The data set does not provide the same information as the TROPOMI Australia data set described in Section 2.1. The errors associated with $HONO/NO_2$, the TROPOMI pixel boundaries, and UVAI are not included, and thus we adjusted our analysis to account for this. For every TROPOMI pixel, we performed descriptive statistics of surrounding TROPOMI pixels and VIIRS FRP pixels within 7 km. We report on the unweighted-mean $HONO/NO_2$ and unweighted-mean FRP.

10.1029/2023GL103836

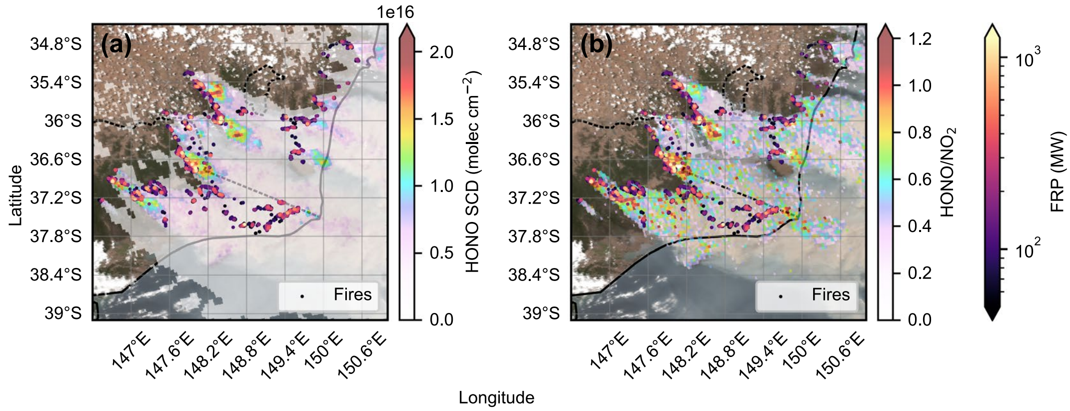

Figure 1. (a) TROPOMI HONO SCD and VIIRS FRP and (b) TROPOMI HONO/NO_2 and VIIRS FRP on 4 January 2020 looking over southeastern Australia. Aqua MODIS surface reflectance imagery is the base layer in both maps. In (a), only UVAI > 0 TROPOMI pixels are plotted, meaning absorbing aerosols are present. In (b), only pixels where HONO and NO_2 SCDs were two times larger than their fit errors are plotted.

3. Results

3.1. Australia

Over our study area and period, the satellites sampled many fires and detected large amounts of HONO and NO_2 in the atmosphere. An example of a satellite scene with HONO SCD and FRP is shown in Figure 1. Figure 2 shows the mean HONO SCD, mean NO_2 SCD, and mean HONO/NO_2 for binned mean FRP over the Australian continent from 1 September 2019, to 31 January 2020 and then divides mean HONO/NO_2 into three land cover groups. In Figure 2, the FRP bins are logarithmically spaced with a constant width (0.1), as more fires have lower FRPs than higher FRPs (Figure S2 in Supporting Information S1), and it more evenly distributes the bin sample sizes. Each bin needs a minimum of 30 pixels to be represented by a boxplot. A total of 5,227 TROPOMI pixels are distributed into eight bins.

As shown in Figures 2b and 2c, mean NO_2 SCDs are larger than mean HONO SCDs. Both the medians and weighted means for these variables increase linearly with mean FRP up to ~200 MW. After this point, mean HONO SCD continues increasing and mean NO_2 SCD stalls. To quantify the observed increases with FRP, a linear function ($y = a \times x +$ b) is fit to the weighted-mean boxplot values in Figure 2. Additional functions are fit to the mean NO_2 SCD binned weighted means because the linear fit fails to capture the shape. For HONO, the linear fit has a coefficient of determination, R^2, of 0.98. For NO_2, the linear fit has an R^2 of 0.81. The mean HONO SCD variability within a mean FRP bin increases relative to that for mean NO_2 SCD with increasing mean FRP, that is, the 25th to 75th percentile distance widens lower than four-fold for HONO but only lower than two-fold for NO_2.

Contrary to the relationship of mean NO_2 SCD, the weighted means of the boxplots for mean HONO/NO_2 increase linearly with mean FRP with a linear function R^2 of 0.97 (Figure 2a). The binned weighted means closely follow the binned medians until a mean FRP of 200 MW. The coefficients for the linear fits can be found in Table 1.

We find that the observed increase of HONO, NO_2, and HONO/NO_2, with increasing FRP is robust against various pixels selections and definitions of quantities (an example of correlation with mean FRP density can be found in Figure S3 in Supporting Information S1). Photochemistry is expected to change in optically thick plumes leading to longer HONO photochemical lifetime and it has been found that NO_x lifetime decreases with increasing fire emissions (Jin et al., 2021). However, Figure S4 in Supporting Information S1 suggests that the increase in HONO SCD relative to that of NO_2 SCD with increasing FRP is related to some extent to the fire power, and thus emissions. This is because the linear relationships for mean HONO/NO_2 do not substantially vary in the slope under different UVAI conditions. However, the intercept increases with increasing UVAI, suggesting that the baseline HONO/NO_2 from fires is affected by the presence of aerosols evenly across all FRP values. Thus, covariations in UVAI will also affect these relationships to some degree. The Australian Black Summer produced multiple pyrocumulonimbus plumes which exhibited UVAI values above 8 at high altitudes in the atmosphere

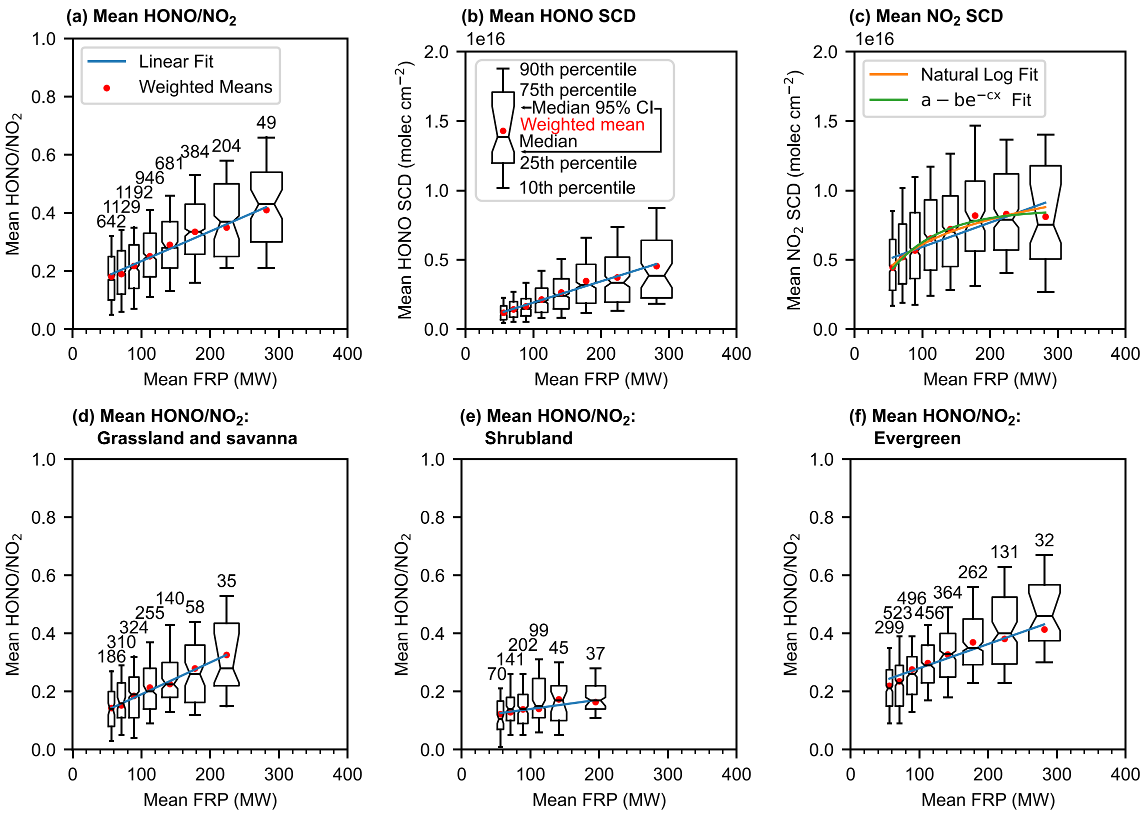

Figure 2. Binned boxplot distributions of (a) mean $HONO/NO_2$, (b) mean HONO SCD, and (c) mean NO_2 SCD for Australia. The gray box in (b) shows that for boxplots black lines are the medians, notches are the median 95% confidence interval, boxes extend from the 25th to 75th percentiles, whiskers extend to the 10th and 90th percentiles, and red-filled circles are the weighted means. Boxplots with more than 30 counts are plotted. A linear function ($y = a \times x + b$) fits the weighted means of each bin and coefficients can be found in Table 1. Since the weighted means in (c) level after 200 MW mean FRP, we performed additional fits. (d)–(f) Same as (a) for different land cover types in Australia: (d) grassland and savanna, (e) shrubland, and (f) evergreen. The last boxplot in (e) shrubland is a combination of the last two bins and is positioned at the average mean FRP.

(Lerot et al., 2023; Peterson et al., 2021). Only 114 of the Australian TROPOMI pixels we sampled had a UVAI greater than 8 (<3% of samples) and thus do not affect our fits. We do not constrain for plume height but acknowledge this could have an influence on $HONO/NO_2$.

Since fire emissions depend on fuel conditions, we investigated the effect that land cover type has on the mean $HONO/NO_2$ and mean FRP relationship. Figure 2d–2f breaks Figure 2a up into three broad land cover categories: grassland and savanna, shrubland, and evergreen. There are 1,308 TROPOMI pixels that are either characterized as grassland or savanna, 594 shrubland TROPOMI pixels, and 2,563 evergreen TROPOMI pixels.

Looking at the bin counts, we find that all biomes share similar profiles, with grassland and savanna, and shrubland plants all reaching their maximums between 79 and 100 MW and the evergreen plants peaking between 63 and 79 MW (Figure 2d–2f). From the binned boxplots, we conclude that evergreen fires have higher mean $HONO/NO_2$ compared to the grassland and savanna, and shrubland fires (consistent with the findings of Theys et al., 2020), and is due to higher mean HONO SCDs (Figure S5 in Supporting Information S1). Both the grassland and savanna, and evergreen land cover types demonstrate good linear relationships with R^2 of 0.99 and 0.94, respectively, while shrubland types have an R^2 of 0.76. In the first FRP bin (50 MW), shrubland fires have the lowest bin mean of all other fires at 0.12, meaning they emit the least HONO per NO_2 molecule. In contrast, evergreen fires have the highest bin mean at 0.22. Shrubland fires have the weakest relationship between mean $HONO/NO_2$ and mean FRP, roughly a factor of three difference between the other fires. Figure 2 demonstrates that it is necessary to consider the land cover type when deriving these relationships. The coefficients for the linear fits can be found in Table 1. A comparison of linear fits between each individual land cover type can be found in Figure S6 in Supporting Information S1.

Table 1
Coefficients of Linear ($y = a \times x + b$) Fits of Different Variables to the Weighted-Mean Binned Values of Mean FRP Plus One Standard Deviation Error

Variable	Coefficient a	Coefficient b	R^2
Mean HONO SCD[a]	1.5 (±0.1) × 10^{13} molec HONO cm^{-2} MW^{-1}	4 (±2) × 10^{14} molec HONO cm^{-2}	0.98
Mean NO_2 SCD[a]	1.8 (±0.3) × 10^{13} molec NO_2 cm^{-2} MW^{-1}	4.2 (±0.6) × 10^{15} molec NO_2 cm^{-2}	0.81
Mean NO_2 SCD $y = a \times \ln(b \times x)$[a]	2.6 (±0.5) × 10^{15} molec NO_2 cm^{-2}	1.1 (±0.5) × 10^{-1} MW^{-1}	0.94
Mean NO_2 SCD $y = a - b \times e^{-c \times x}$[a,b]	8.6 (±0.9) × 10^{15} molec NO_2 cm^{-2}	9 (±4) × 10^{15} molec NO_2 cm^{-2}	0.98
Mean HONO/NO_2	1.0 (±0.2) × 10^{-3} MW^{-1}	1.3 (±0.4) × 10^{-1}	0.97
Grassland and savanna mean HONO/NO_2	1.1 (±0.3) × 10^{-3} MW^{-1}	0.8 (±0.5) × 10^{-1}	0.99
Shrubland mean HONO/NO_2	3 (±4) × 10^{-4} MW^{-1}	1.1 (±0.4) × 10^{-1}	0.76
Evergreen mean HONO/NO_2	8 (±2) × 10^{-4} MW^{-1}	2.0 (±0.4) × 10^{-1}	0.94
Global mean HONO/NO_2	5.7 (±0.8) × 10^{-4} MW^{-1}	3.1 (±0.2) × 10^{-1}	0.87
Global grassland and savanna mean HONO/NO_2	1.1 (±0.1) × 10^{-3} MW^{-1}	2.3 (±0.2) × 10^{-1}	0.91
Global shrubland mean HONO/NO_2	9 (±2) × 10^{-4} MW^{-1}	2.0 (±0.3) × 10^{-1}	0.94
Global evergreen mean HONO/NO_2	8 (±2) × 10^{-4} MW^{-1}	3.6 (±0.3) × 10^{-1}	0.83

Note. Values reported in this table are for Australian fires. Global fires are labeled separately. Fits that are nonlinear are indicated. R^2 is the coefficient of determination.
[a]Fits are for demonstration only. Varying fire characteristics affect SCDs substantially. [b]Coefficient c is 1.4 (±0.8) × 10^{-2} MW^{-1}.

3.2. Global

We expanded our investigation to the entire globe to test if our Australian-derived relationships hold for the rest of the world. There are 2,449 datapoints in the global data set after applying the filtering method. The same land cover type categories shown in Figures 2d–2f are displayed in Figures 3b–3d, where there are 1,191 global TROPOMI pixels categorized as grassland or savanna, 122 global TROPOMI pixels categorized as shrubland, and 233 global TROPOMI pixels categorized as evergreen. Contrary to the Australian wildfire data set, there are more observations of grassland and savanna fires than evergreen fires.

As shown in Table 1, the slope between mean HONO/NO_2 and mean FRP in the global all-land-cover-type data set is 56% of the slope in the Australian data set, demonstrating a more complicated relationship between the two variables. The linear fit is weaker with an R^2 of 0.87 but is due to the nonlinear response of the bin means. The bin means follow more of a sigmoid response, perhaps indicating the existence of two solution states depending on the value of mean FRP. This sigmoid response is also seen in the global grassland and savanna fires in Figure 3b. Even though the global data set mixes many different regions and fire seasons across the world, the slopes of the grassland and savanna, and evergreen land cover type relationships agree well with those relationships derived from Australia. Conclusions about the global shrublands land cover type cannot be made as only three FRP bins had enough samples to perform a fitting. Results from each individual land cover type can be found in Figure S7 in Supporting Information S1. A general conclusion from this analysis is the overall HONO/NO_2 increase with increasing FRP. The similarities in relationships between the world and Australia calls for a more detailed analysis for all regions of the world.

4. Conclusions

Based on satellite measurements, we found a consistent increasing linear relationship between the ratio of HONO to NO_2 and FRP over the 2019–2020 fires in Australia. Moreover, the linear regression fit parameters were found to vary with land cover type. By extending the analysis to the entire world, these relationships differ, but the overall increasing relationship remains. This suggests there is increased production of HONO under flaming combustion, though the impacts of smoke on increased HONO lifetime cannot be ignored, as UVAI impacted the regression intercepts. We have placed bounds on the HONO/NO_2 versus FRP both in Australia and globally. However, we recommend using these relationships for fires with FRP under 400 MW, and for fires above 400 MW to use a maximum HONO/NO_2 of 1, as 90% of HONO/NO_2 was less than 1. We do not have the statistics to support conclusions about larger fires and satellite footprints may not be small enough to resolve these fires, thus future work is needed to analyze large individual fires. Our results support future HONO emissions estimations from fires, where parameterized, first-order HONO emissions estimates require a land-cover-type- and FRP-dependent multiplier to the estimate of NO_2 emissions. This framework would work well with emissions methods that utilize satellite FRP measurements but lack HONO emission factors, such as the Quick Fire Emission Dataset (QFED) from NASA (Darmenov & da Silva, 2015) or the Global Fire Assimilation (GFAS) (Kaiser et al., 2012). An accurate description of HONO emissions from fires is critical to understanding and modeling the impacts of wildfire smoke on atmospheric chemistry.

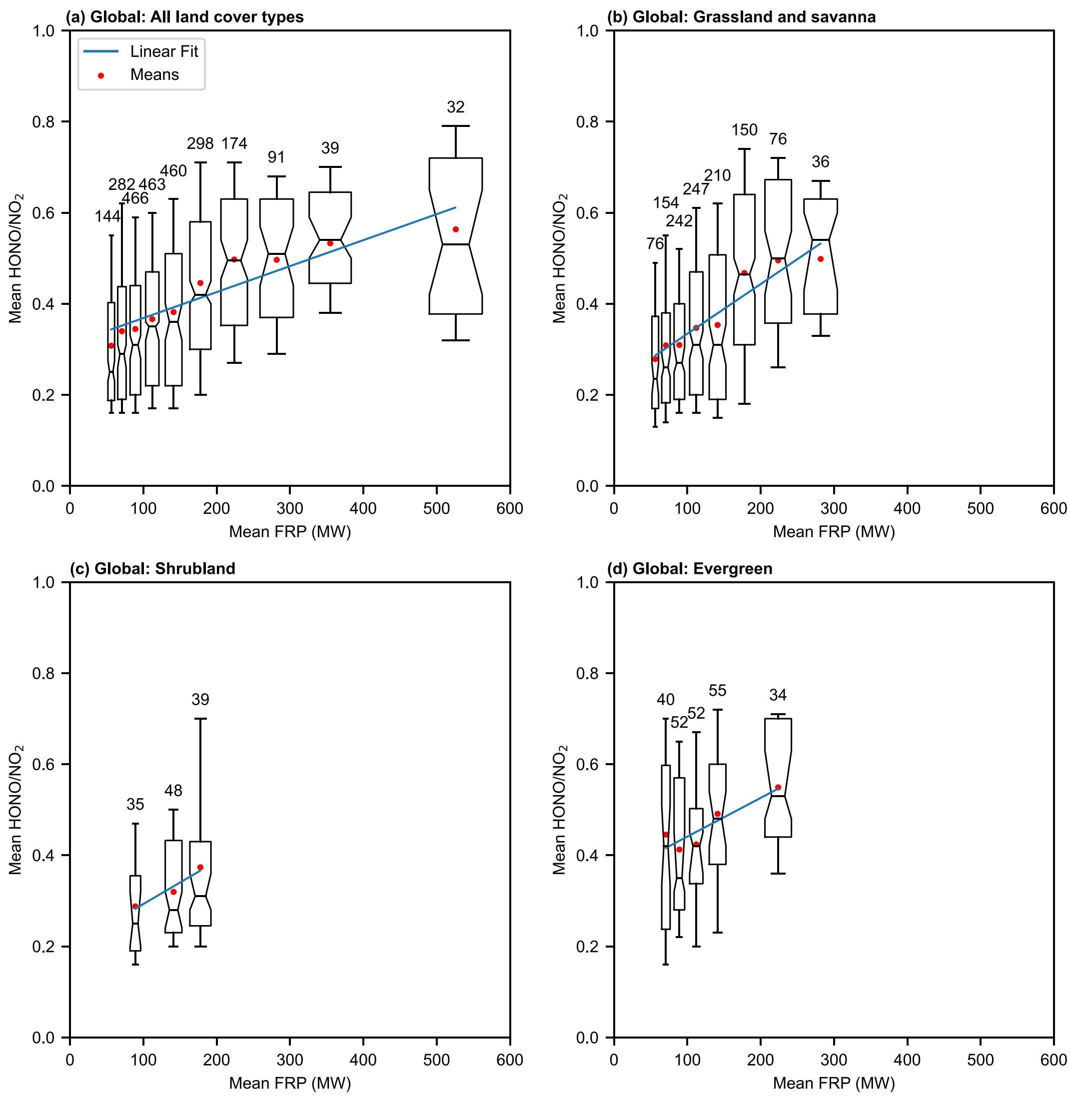

Figure 3. Binned boxplot distributions of mean $HONO/NO_2$ against mean FRP for (a) global, (b) global grassland and savanna, (c) global shrubland, and (d) global evergreen fires. The boxplot symbology is the same as Figure 2, except red circles are now unweighted bin means. Boxplots with more than 30 counts are plotted. A linear function ($y = a \times x + b$) is fit to the means of each bin and its coefficients can be found in Table 1. In (a), fires above a mean FRP of 398 MW were grouped together and plotted at the average mean FRP.

Conflict of Interest

The authors declare no conflicts of interest relevant to this study.

Data Availability Statement

The Australia and global data used for Figures 1–3 in the study are available at Open Science Framework via https://doi.org/10.17605/OSF.IO/2SP49 (Fredrickson & Thornton, 2023). The filtered Suomi NPP fire data in the study were downloaded from NASA FIRMS via their API area tool at https://firms.modaps.eosdis.nasa.gov/api/area/. MODIS Land Cover Type Version 6 data were acquired through Google Earth Engine via https://doi.org/10.5067/MODIS/MCD12Q1.006. The Jupyter notebook with Python code used to execute this project is preserved at https://doi.org/10.5281/zenodo.7782598 available via the MIT license (Fredrickson, 2023).

Acknowledgments

CDF acknowledges the National Aeronautics and Space Administration with the Future Investigators in NASA Earth and Space Science and Technology (FINESST) Grant 80NSSC20K1612 for supporting this project. JAT acknowledges support from the U.S. National Science Foundation (AGS-1652688). NT acknowledges financial support from the European Space Agency DINAR (Development and Interpretation of Improved Nitrous Acid Retrievals) project Contract No. 4000137831/22/I-AG. This paper contains modified Copernicus data (2018–2020) processed by BIRA-IASB. We acknowledge the use of data and/or imagery from NASA's Fire Information for Resource Management System (FIRMS) (https://earthdata.nasa.gov/firms), part of NASA's Earth Observing System Data and Information System (EOSDIS). The authors would like to thank Becky Alexander, Ernesto Alvarado, Lyatt Jaeglé, and Alex Turner for their feedback on this project.

References

Barbero, R., Abatzoglou, J. T., Larkin, N. K., Kolden, C. A., & Stocks, B. (2015). Climate change presents increased potential for very large fires in the contiguous United States. *International Journal of Wildland Fire*, *24*(7), 892. https://doi.org/10.1071/WF15083

Barney, W. S., Wingen, L. M., Lakin, M. J., Brauers, T., Stutz, J., & Finlayson-Pitts, B. J. (2000). Infrared absorption cross-section measurements for nitrous acid (HONO) at room temperature. *The Journal of Physical Chemistry A*, *104*(8), 1692–1699. https://doi.org/10.1021/jp9930503

Bernath, P., Boone, C., & Crouse, J. (2022). Wildfire smoke destroys stratospheric ozone. *Science*, *375*(6586), 1292–1295. https://doi.org/10.1126/science.abm5611

Bourgeois, I., Peischl, J., Neuman, J. A., Brown, S. S., Allen, H. M., Campuzano-Jost, P., et al. (2022). Comparison of airborne measurements of NO, NO_2, HONO, NOy, and CO during FIREX-AQ. *Atmospheric Measurement Techniques*, *15*(16), 4901–4930. https://doi.org/10.5194/amt-15-4901-2022

Bousserez, N. (2014). Space-based retrieval of NO_2 over biomass burning regions: Quantifying and reducing uncertainties. *Atmospheric Measurement Techniques*, *7*(10), 3431–3444. https://doi.org/10.5194/amt-7-3431-2014

Burling, I. R., Yokelson, R. J., Griffith, D. W. T., Johnson, T. J., Veres, P., Roberts, J. M., et al. (2010). Laboratory measurements of trace gas emissions from biomass burning of fuel types from the southeastern and southwestern United States. *Atmospheric Chemistry and Physics*, *10*(22), 11115–11130. https://doi.org/10.5194/acp-10-11115-2010

Chai, J., Miller, D. J., Scheuer, E., Dibb, J., Selimovic, V., Yokelson, R., et al. (2019). Isotopic characterization of nitrogen oxides (NO_x), nitrous acid (HONO), and nitrate ($p\mathrm{NO_3}^-$) from laboratory biomass burning during FIREX. *Atmospheric Measurement Techniques*, *12*(12), 6303–6317. https://doi.org/10.5194/amt-12-6303-2019

Chen, L.-W. A., Verburg, P., Shackelford, A., Zhu, D., Susfalk, R., Chow, J. C., & Watson, J. G. (2010). Moisture effects on carbon and nitrogen emission from burning of wildland biomass. *Atmospheric Chemistry and Physics*, *10*(14), 6617–6625. https://doi.org/10.5194/acp-10-6617-2010

Coggon, M. M., Veres, P. R., Yuan, B., Koss, A., Warneke, C., Gilman, J. B., et al. (2016). Emissions of nitrogen-containing organic compounds from the burning of herbaceous and arboraceous biomass: Fuel composition dependence and the variability of commonly used nitrile tracers. *Geophysical Research Letters*, *43*(18), 9903–9912. https://doi.org/10.1002/2016GL070562

Darmenov, A., & da Silva, A. (2015). *The quick fire emissions dataset (QFED): Documentation of versions 2.1, 2.2 and 2.4*. (NASA/TM-2015-104606/Vol. 38; Technical Report Series on Global Modeling and Data Assimilation, Volume 38). NASA Goddard Space Flight Center. Retrieved from https://gmao.gsfc.nasa.gov/pubs/docs/Darmenov796.pdf

Dennison, P. E., Brewer, S. C., Arnold, J. D., & Moritz, M. A. (2014). Large wildfire trends in the western United States, 1984-2011. *Geophysical Research Letters*, *41*(8), 2928–2933. https://doi.org/10.1002/2014GL059576

Elshorbany, Y. F., Kleffmann, J., Hofzumahaus, A., Kurtenbach, R., Wiesen, P., Brauers, T., et al. (2012). HOx budgets during HOxComp: A case study of HOx chemistry under NOx-limited conditions. *Journal of Geophysical Research*, *117*(D3), D03307. https://doi.org/10.1029/2011JD017008

Fredrickson, C. (2023). cdfredrickson/Satellite-HONO-NO2-FRP: Satellite HONO NO2 FRP Release (v1.0.0) [Software]. Zenodo. https://doi.org/10.5281/ZENODO.7782599

Fredrickson, C., & Thornton, J. A. (2023). TROPOMI HONO/NO2 Australian fires [Dataset]. Open Science Framework. https://doi.org/10.17605/OSF.IO/2SP49

Friedl, M., & Sulla-Menashe, D. (2019). MCD12Q1 MODIS/Terra+Aqua land cover type yearly L3 global 500m SIN grid V006 [Dataset]. NASA EOSDIS Land Processes DAAC. https://doi.org/10.5067/MODIS/MCD12Q1.006

Gil, J., Kim, J., Lee, M., Lee, G., Ahn, J., Lee, D. S., et al. (2021). Characteristics of HONO and its impact on O_3 formation in the Seoul Metropolitan area during the Korea-US air quality study. *Atmospheric Environment*, *247*, 118182. https://doi.org/10.1016/j.atmosenv.2020.118182

Jin, X., Zhu, Q., & Cohen, R. C. (2021). Direct estimates of biomass burning NOx emissions and lifetimes using daily observations from TROPOMI. *Atmospheric Chemistry and Physics*, *21*(20), 15569–15587. https://doi.org/10.5194/acp-21-15569-2021

Juncosa Calahorrano, J. F., Lindaas, J., O'Dell, K., Palm, B. B., Peng, Q., Flocke, F., et al. (2021). Daytime oxidized reactive nitrogen partitioning in western U.S. wildfire smoke plumes. *Journal of Geophysical Research: Atmospheres*, *126*(4), e2020JD033484. https://doi.org/10.1029/2020JD033484

Kaiser, J. W., Heil, A., Andreae, M. O., Benedetti, A., Chubarova, N., Jones, L., et al. (2012). Biomass burning emissions estimated with a global fire assimilation system based on observed fire radiative power. *Biogeosciences*, *9*(1), 527–554. https://doi.org/10.5194/bg-9-527-2012

Kleffmann, J. (2007). Daytime sources of nitrous acid (HONO) in the atmospheric boundary layer. *ChemPhysChem*, *8*(8), 1137–1144. https://doi.org/10.1002/cphc.200700016

Lerot, C., Müller, J.-F., Theys, N., De Smedt, I., Stavrakou, T., & Van Roozendael, M. (2023). Satellite evidence for glyoxal depletion in elevated fire plumes. *Geophysical Research Letters*, *50*(4), e2022GL102195. https://doi.org/10.1029/2022GL102195

Lin, J.-T., Liu, M.-Y., Xin, J.-Y., Boersma, K. F., Spurr, R., Martin, R., & Zhang, Q. (2015). Influence of aerosols and surface reflectance on satellite NO2 retrieval: Seasonal and spatial characteristics and implications for NOx emission constraints. *Atmospheric Chemistry and Physics*, *15*(19), 11217–11241. https://doi.org/10.5194/acp-15-11217-2015

Lindaas, J., Pollack, I. B., Garofalo, L. A., Pothier, M. A., Farmer, D. K., Kreidenweis, S. M., et al. (2021). Emissions of reactive nitrogen from western U.S. wildfires during summer 2018. *Journal of Geophysical Research: Atmospheres*, *126*(2), e2020JD032657. https://doi.org/10.1029/2020JD032657

Mouat, A. P., Paton-Walsh, C., Simmons, J. B., Ramirez-Gamboa, J., Griffith, D. W. T., & Kaiser, J. (2022). Measurement report: Observations of long-lived volatile organic compounds from the 2019–2020 Australian wildfires during the COALA campaign. *Atmospheric Chemistry and Physics*, *22*(17), 11033–11047. https://doi.org/10.5194/acp-22-11033-2022

Müller, M., Anderson, B. E., Beyersdorf, A. J., Crawford, J. H., Diskin, G. S., Eichler, P., et al. (2016). In situ measurements and modeling of reactive trace gases in a small biomass burning plume. *Atmospheric Chemistry and Physics*, *16*(6), 3813–3824. https://doi.org/10.5194/acp-16-3813-2016

Neuman, J. A., Trainer, M., Brown, S. S., Min, K.-E., Nowak, J. B., Parrish, D. D., et al. (2016). HONO emission and production determined from airborne measurements over the Southeast U.S. *Journal of Geophysical Research: Atmospheres*, *121*(15), 9237–9250. https://doi.org/10.1002/2016JD025197

Peng, Q., Palm, B. B., Fredrickson, C. D., Lee, B. H., Hall, S. R., Ullmann, K., et al. (2022). Direct constraints on secondary HONO production in aged wildfire smoke from airborne measurements over the western US. *Geophysical Research Letters*, *49*(15), e2022GL098704. https://doi.org/10.1029/2022GL098704

Peng, Q., Palm, B. B., Melander, K. E., Lee, B. H., Hall, S. R., Ullmann, K., et al. (2020). HONO emissions from western U.S. wildfires provide dominant radical source in fresh wildfire smoke. *Environmental Science & Technology*, *54*(10), 5954–5963. https://doi.org/10.1021/acs.est.0c00126

Penning de Vries, M. J. M., Beirle, S., & Wagner, T. (2009). UV aerosol indices from SCIAMACHY: Introducing the SCattering Index (SCI). *Atmospheric Chemistry and Physics*, *9*(24), 9555–9567. https://doi.org/10.5194/acp-9-9555-2009

Peterson, D. A., Fromm, M. D., McRae, R. H. D., Campbell, J. R., Hyer, E. J., Taha, G., et al. (2021). Australia's Black Summer pyrocumulonimbus super outbreak reveals potential for increasingly extreme stratospheric smoke events. *Npj Climate and Atmospheric Science*, *4*(1), 38. https://doi.org/10.1038/s41612-021-00192-9

Platt, U., & Stutz, J. (2008). Differential absorption spectroscopy. In *Differential optical absorption spectroscopy* (pp. 135–174). Springer Berlin Heidelberg. https://doi.org/10.1007/978-3-540-75776-4_6

Roberts, J. M., Stockwell, C. E., Yokelson, R. J., de Gouw, J., Liu, Y., Selimovic, V., et al. (2020). The nitrogen budget of laboratory-simulated western US wildfires during the FIREX 2016 Fire Lab study. *Atmospheric Chemistry and Physics*, *20*(14), 8807–8826. https://doi.org/10.5194/acp-20-8807-2020

Rondon, A., & Sanhueza, E. (1989). High HONO atmospheric concentrations during vegetation burning in the tropical savannah. *Tellus B: Chemical and Physical Meteorology*, *41*(4), 474. https://doi.org/10.3402/tellusb.v41i4.15102

Rowe, J. P., Zarzana, K. J., Kille, N., Borsdorff, T., Goudar, M., Lee, C. F., et al. (2022). Carbon monoxide in optically thick wildfire smoke: Evaluating TROPOMI using CU airborne SOF column observations. *ACS Earth and Space Chemistry*, *6*(7), 1799–1812. https://doi.org/10.1021/acsearthspacechem.2c00048

Schroeder, W. (2020). VIIRS (S-NPP) I band 375 m active fire locations NRT (vector data) [Dataset]. NASA Land Atmosphere Near real-time Capability for EOS Fire Information for Resource Management System. https://doi.org/10.5067/FIRMS/VIIRS/VNP14IMGT_NRT.002

Schroeder, W., Csiszar, I., Giglio, L., & Schmidt, C. C. (2010). On the use of fire radiative power, area, and temperature estimates to characterize biomass burning via moderate to coarse spatial resolution remote sensing data in the Brazilian Amazon. *Journal of Geophysical Research*, *115*(D21), D21121. https://doi.org/10.1029/2009JD013769

Schroeder, W., Oliva, P., Giglio, L., & Csiszar, I. A. (2014). The New VIIRS 375 m active fire detection data product: Algorithm description and initial assessment. *Remote Sensing of Environment*, *143*, 85–96. https://doi.org/10.1016/j.rse.2013.12.008

Simmons, J. B., Paton-Walsh, C., Mouat, A. P., Kaiser, J., Humphries, R. S., Keywood, M., et al. (2022). Bushfire smoke plume composition and toxicological assessment from the 2019–2020 Australian Black Summer. *Air Quality, Atmosphere & Health*, *15*(11), 2067–2089. https://doi.org/10.1007/s11869-022-01237-5

Solomon, S., Dube, K., Stone, K., Yu, P., Kinnison, D., Toon, O. B., et al. (2022). On the stratospheric chemistry of midlatitude wildfire smoke. *Proceedings of the National Academy of Sciences*, *119*(10), e2117325119. https://doi.org/10.1073/pnas.2117325119

Solomon, S., Stone, K., Yu, P., Murphy, D. M., Kinnison, D., Ravishankara, A. R., & Wang, P. (2023). Chlorine activation and enhanced ozone depletion induced by wildfire aerosol. *Nature*, *615*(7951), 259–264. https://doi.org/10.1038/s41586-022-05683-0

Souri, A. H., Choi, Y., Jeon, W., Kochanski, A. K., Diao, L., Mandel, J., et al. (2017). Quantifying the impact of biomass burning emissions on major inorganic aerosols and their precursors in the U.S.: Burning impact on inorganic aerosols. *Journal of Geophysical Research: Atmospheres*, *122*(21), 12020–12041. https://doi.org/10.1002/2017JD026788

Stein Zweers, D. C. (2022). TROPOMI ATBD of the UV aerosol index. (No. S5P-KNMI-L2-0008-RP) (pp. 1–30). Retrieved from https://sentinel.esa.int/documents/247904/2476257/Sentinel-5P-TROPOMI-ATBD-UV-Aerosol-Index.pdf

Stockwell, C. E., Yokelson, R. J., Kreidenweis, S. M., Robinson, A. L., DeMott, P. J., Sullivan, R. C., et al. (2014). Trace gas emissions from combustion of peat, crop residue, domestic biofuels, grasses, and other fuels: Configuration and Fourier transform infrared (FTIR) component of the fourth Fire Lab at Missoula Experiment (FLAME-4). *Atmospheric Chemistry and Physics*, *14*(18), 9727–9754. https://doi.org/10.5194/acp-14-9727-2014

Stockwell, W. R., & Calvert, J. G. (1978). The near ultraviolet absorption spectrum of gaseous HONO and N2O3. *Journal of Photochemistry*, *8*(2), 193–203. https://doi.org/10.1016/0047-2670(78)80019-7

Theys, N., Volkamer, R., Müller, J.-F., Zarzana, K. J., Kille, N., Clarisse, L., et al. (2020). Global nitrous acid emissions and levels of regional oxidants enhanced by wildfires. *Nature Geoscience*, *13*(10), 681–686. https://doi.org/10.1038/s41561-020-0637-7

Wang, S., Coggon, M. M., Gkatzelis, G. I., Warneke, C., Bourgeois, I., Ryerson, T., et al. (2021). Chemical tomography in a fresh wildland fire plume: A large eddy simulation (LES) study. *Journal of Geophysical Research: Atmospheres*, *126*(18), e2021JD035203. https://doi.org/10.1029/2021JD035203

Yokelson, R. J., Crounse, J. D., DeCarlo, P. F., Karl, T., Urbanski, S., Atlas, E., et al. (2009). Emissions from biomass burning in the Yucatan. *Atmospheric Chemistry and Physics*, *9*(15), 5785–5812. https://doi.org/10.5194/acp-9-5785-2009

Yokelson, R. J., Karl, T., Artaxo, P., Blake, D. R., Christian, T. J., Griffith, D. W. T., et al. (2007). The tropical forest and fire emissions experiment: Overview and airborne fire emission factor measurements. *Atmospheric Chemistry and Physics*, *7*(19), 5175–5196. https://doi.org/10.5194/acp-7-5175-2007

Zhang, J., Guo, Y., Qu, Y., Chen, Y., Yu, R., Xue, C., et al. (2020). Effect of potential HONO sources on peroxyacetyl nitrate (PAN) formation in eastern China in winter. *Journal of Environmental Sciences*, *94*, 81–87. https://doi.org/10.1016/j.jes.2020.03.039

Zhang, S., Sarwar, G., Xing, J., Chu, B., Xue, C., Sarav, A., et al. (2021). Improving the representation of HONO chemistry in CMAQ and examining its impact on haze over China. *Atmospheric Chemistry and Physics*, *21*(20), 15809–15826. https://doi.org/10.5194/acp-21-15809-2021